# Amplification of laser imprint in the presence of strong, externally imposed, target-normal magnetic fields

Luke Ceurvorst,<sup>1,\*</sup> Christopher Walsh,<sup>2</sup> Gabriel Pérez-Callejo,<sup>3</sup> Victorien Bouffetier,<sup>4</sup> Philip Bradford,<sup>5</sup> Jonathan L. Peebles,<sup>1</sup> Suxing Hu,<sup>1</sup> Wolfgang Theobald,<sup>1</sup> and Alexis Casner<sup>6</sup>

<sup>1</sup>Laboratory for Laser Energetics, University of Rochester, Rochester, NY 14623-1299, USA

<sup>2</sup>Lawrence Livermore National Laboratory, Livermore, CA 94550, USA

<sup>3</sup>Departamento de Físca Teórica, Atómica y Óptica, Universidad de Valladolid, Valladolid, Spain

<sup>4</sup>European XFEL, Schenefeld, Germany

<sup>5</sup>Centre Lasers Intenses et Applications, Université de Bordeaux-CNRS-CEA, Bordeaux, France

<sup>6</sup>Commissariat a L'Energie Atomique CESTA, le Barp, France

(Dated: August 8, 2025)

An experiment was performed on the OMEGA EP Laser System to investigate the effects of magnetic fields on laser imprint. A 30-µm-thick CH target was driven by a single beam delivering 3.0 kJ of UV energy in a 5-ns square pulse without smoothing by spectral dispersion. The Rayleigh-Taylor amplification of this beam's imprint on the target surface was monitored using face-on gated x-ray radiography from a Gd backlighter. Magnetic fields of up to 45 T were applied normal to the target surface. Analysis of the resulting radiographs shows a  $60 \pm 13\%$  increase in the spectrally resolved surface perturbation amplitudes, consistent at all times and for all unsaturated frequencies. This consistency indicates that the increase in perturbation amplitudes was due to a change in the initial amplitudes rather than Rayleigh-Taylor growth. This is supported by the trajectory of individual modes and the inferred time-averaged perturbation growth rates. Laser imprint is therefore inferred to have increased due to strong magnetic fields that remain in the conduction zone of the target, suppressing off-axis electron motion and limiting the effects of thermal smoothing.

## I. INTRODUCTION

To reach net energy gain in inertial confinement fusion (ICF) [1–3], a capsule consisting of cryogenic deuterium and tritium must be efficiently compressed to high areal densities and temperatures. If the  $\alpha$  particles produced by the D-T reactions are confined to the compressed core, they deposit their energy and produce a burn wave that ignites the capsule. The released energy of this burn can exceed the energy driving the implosion.

One approach to enhance  $\alpha$ -particle confinement and suppress thermal conduction is to magnetize the ICF capsule [4]. By magnetically trapping the ions, lower implosion velocities can be used while still achieving ignition-relevant conditions, improving overall energy gain [5]. Doing so requires fields of the order of a kilotesla during the nuclear burn stage. Such enormous field strengths can be achieved via magnetic-flux compression. A field of the order of 10 T is applied to the target prior to compression. During the drive, the field lines are locked into the inner ionized vapor, amplifying the compressed field strength by factors of  $10^3$  as the shell converges [6–8].

Previous experiments conducted on the OMEGA laser have verified these effects using moderate initial field strengths. Cylindrical implosions demonstrated the compression of magnetic fields, amplifying an initial strength of 10 T to 3 to 4 kT, consistent with frozen-field estimates [6, 9]. Subsequent spherical implosions imposed an 8-T magnetic field along the axis of a polar-direct-drive im-

plosion and increased both yield and ion temperature by 30% and f, respectively [5].

Despite these promising early results, challenges arise at greater initial field strengths. Recent exploding-pusher experiments conducted on OMEGA demonstrated a significant increase in low-mode asymmetries in the presence of a 50 T imposed field [10]. This field strength was strong enough to magnetize the electron species, leading to significantly suppressed heat conduction along the equator of the target perpendicular to the field lines and resulting in an oblate implosion. Rather than increasing yields, the magnetically induced asymmetries caused yields to fall by  $\sim 23\%$ . This loss may be somewhat recovered through beam pointing, power balance, and target shaping [11, 12].

In addition to complicating symmetry control, a recent numerical study indicates that strong magnetic fields can increase laser imprint [13]. To understand this mechanism, it is important to first understand the underlying physics of laser imprint. This phenomenon is an issue in any direct-drive implosion [11, 14] and occurs when a laser beam impinges directly on a target, transferring its speckled spatial modulations to the target's surface [15]. High-intensity speckles increase ablation pressure relative to their surrounding low-intensity troughs, resulting in a warped shock front into the unablated mass that stretches the material surface behind it [11]. However, as the laser drive continues, the absorption region of the laser pulse is pushed away from the ablation front due to plasma expansion. Rather than being directly deposited at the ablation front, energy is conducted from the absorption region via the electron species through a volume known as the conduction zone. Under normal

<sup>\*</sup> lceurvorst@lle.rochester.edu

conditions, electrons move off of the target-normal axis through the conduction zone, spreading the energy from a single laser speckle over a large region of the ablation front. This thermal smoothing mitigates laser imprint, reducing the pressure perturbations exponentially with the depth of the conduction zone [16]. However, when strong magnetic fields exist in the conduction zone normal to the target's surface, electron motion across the field lines is suppressed. This reduces the electron spreading, thereby minimizing thermal smoothing and increasing imprint amplitudes. When modeled using Gorgon magnetohydrodynamic simulations with an initial field strength of 50 T, it was found that imprint was amplified across a wide range of perturbation modes by up to an order of magnitude [13]. Thanks to advancements to the Magneto-Inertial Fusion Electrical Discharge System (MIFEDS) at the Omega Laser Facility, such field strengths are now achievable in the laboratory [17]. This paper presents the results of a planar experiment carried out on OMEGA EP [18] designed to observe the magnetic amplification of laser imprint.

#### II. EXPERIMENTAL SETUP

A schematic of the experiment is shown in Fig. 1. A 30-µm-thick CH disk was placed at target chamber center where it was driven by 3.0 kJ of ultraviolet (UV, 351 nm) laser light in a 5 ns square pulse. A distributed phase plate produced a roughly 750-µm-diameter spot for an on-target intensity of  $1.8 \times 10^{14} \, \mathrm{W/cm^2}$ . No smoothing by spectral dispersion [19] (SSD) was applied, allowing the laser pulse's spatial modulations to be imprinted onto the target's surface. MIFEDS was used on some shots to generate  $45 \pm 5 \, \mathrm{T}$  magnetic fields normal to the target's surface. This system discharges electrical energy stored in capacitors through a coil near the target, inducing a magnetic field. Additionally, shot 38190 had a field strength of  $25\pm5 \, \mathrm{T}$ , providing an intermediate data point.

The target was driven by the long UV pulse as the low-density ablated plasma expanded off of the high-density bulk target. Simulations and previous experiments with similar setups have shown that this causes the target to accelerate after approximately 1 ns of drive. [20] Upon acceleration, such a system is Rayleigh-Taylor (RT) unstable [21], and, in the linear regime, the initial laser-imprinted seed perturbations grow exponentially in time [22] to levels detectable by x-ray radiography. The Betti-Takabe growth rate for ablative Rayleigh-Taylor growth is given by: [22]

$$\gamma_{\rm BT} = A\sqrt{\frac{kg}{1 + kL_{\rm min}}} - BkV_a \tag{1}$$

where A and B are constants (0.98 and 1.7 respectively for CH ablators),[23] k is the perturbation wave number, g is the acceleration of the interface,  $L_{\min}$  is the minimum density scale length at the ablation front, and  $V_a$  is the ablation velocity. For targets and laser drives such as

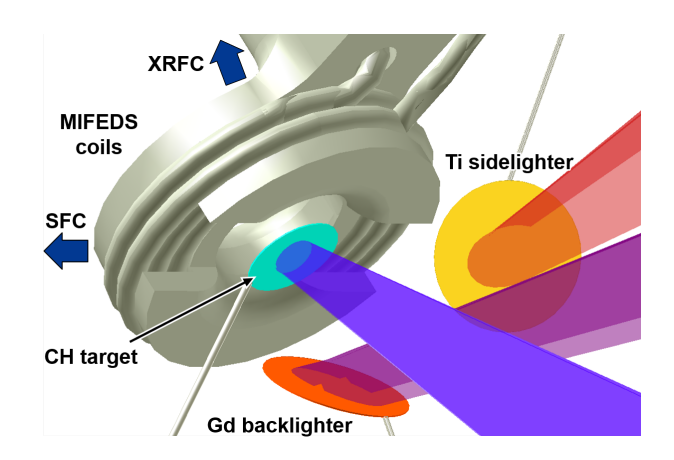


FIG. 1. Experiment schematic showing the primary target (teal disk), Gd backlighter (red disk), and Ti sidelighter (yellow disk) driven by their respective laser pulses. The MIFEDS coils are shown in gray. Arrows indicate the directions of the framing cameras.

Time (ns)	0 T	$25\mathrm{T}$	$45\mathrm{T}$
1.2	4	1	1
1.6	0	0	1
2.0	4	1	1
2.4	2	0	2
2.8	5	1	2
3.2	2	0	2
3.6	5	1	1
4.0	1	0	1
4.8	1	0	1

TABLE I. Number of shots of an applied magnetic-field strength (columns) capturing a given strip timing (rows).

those used in this experiment, typical values are  $g\sim 50\,\mu\text{m/ns}^2$ ,  $L_{\rm min}\sim 10\,\mu\text{m}$ , and  $V_a\sim 2\,\mu\text{m/ns}.[20]$ 

To diagnose the areal-density modulations in the CH target, a Gd backlighter foil was driven by a second UV beam at  $1.1 \times 10^{14} \,\mathrm{W/cm^2}$  for 3 ns, producing quasi-monochromatic radiation at approximately 1.4 keV. These x rays probed the target at 16° off of target normal, passed through the central opening of the MIFEDS assembly, and were collected by a  $4 \times 4$  array of 10-µm-diameter pinholes. These pinholes imaged the data onto an x-ray framing camera (XRFC) with a four-strip microchannel plate to produce an array of sixteen sub-images [24]. The timing of the XRFC strips was varied to capture data from 1.2 ns to 4.8 ns into the main drive in  $0.4\,\mathrm{ns}$  increments with four such times captured per shot. On the final three shots of the experiment, a second backlighter was included, this one consisting of a 25-µm-thick Ti foil driven by a UV beam at  $9.5 \times 10^{13} \,\mathrm{W/cm^2}$  for  $4 \,\mathrm{ns}$  to produce  $4.7 \mathrm{-keV}$  x rays. These x rays passed transversely through the target and were collected by a Sydor framing camera (SFC) to produce side-on x-ray radiographs. A notch was created in the MIFEDS assembly to provide 500 µm clearance to

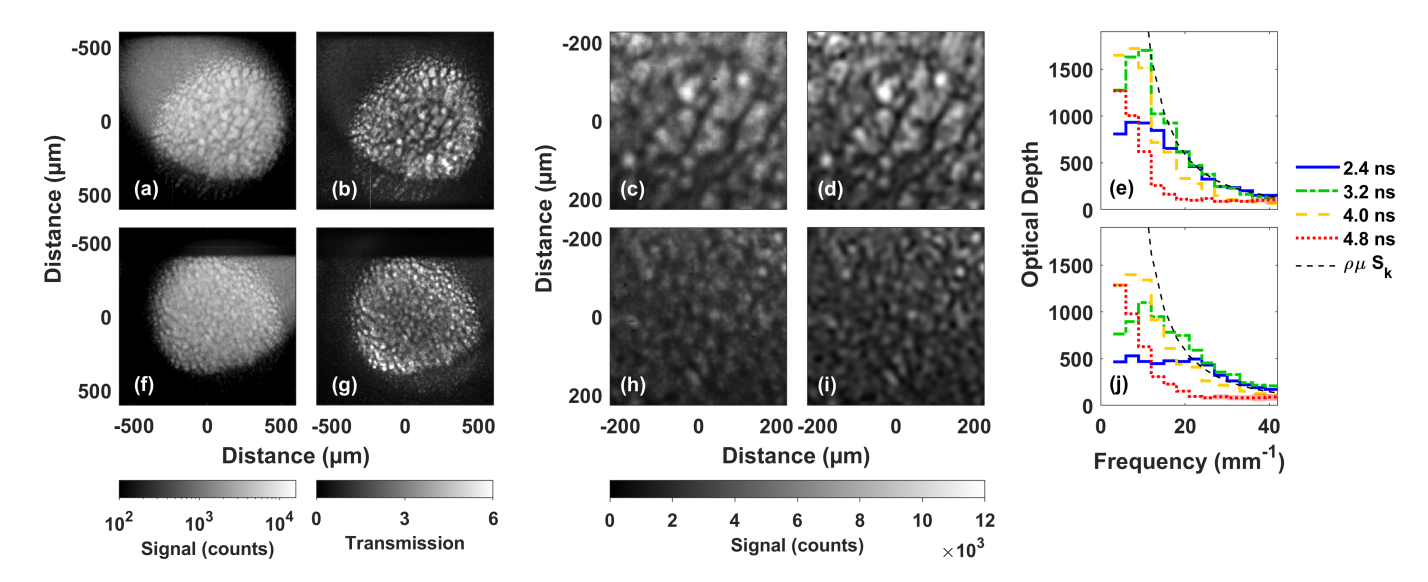


FIG. 2. Analysis of face-on radiography. The analysis process is shown at 2.4 ns for (a)-(e) shot 38191 with 45 T imposed B fields and (f)-(j) shot 38192 with no imposed B fields. (a),(f) Raw radiographs are shown in logarithmic scale to highlight the undriven backlit portion of the target. Also shown are (b),(g) the fitted transmission profiles normalized to the undriven region of the target; (c),(h) the cropped and correlated radiographic signals; (d),(i) the deconvolved radiographic signals; and (e),(j) the average Fourier spectra of the deconvolved optical depth images at every strip timing for each shot. The shaded regions (typically thinner than the line width) indicate the variability of these measurements for each strip. The estimated Haan saturation limit is included with the spectra for visual reference.

observe the target's displacement.

A total of ten shots were performed, six without magnetic fields, one with a 25 T field, and three with 45 T fields. The majority of shots were taken without any effective magnetic field due to technical challenges with the MIFEDS coils. The distribution of shots capturing a specific strip timing is given in Table I. Each strip contains four radiographic images. As described in the subsequent section, adjacent pairs of images within a strip were analyzed together to give signal and noise profiles for a total of 120 analyzed spectra. The figures presented herein average these spectra to summarize the results.

## III. DATA AND IMAGE ANALYSIS

Example face-on radiographs are shown in Figs. 2(a) and 2(f). The backlit regions are highly perturbed where the targets were driven. As low-density RT bubbles expand into the bulk of the target, the line-integrated density goes down, resulting in increased transmission. Conversely, high-density RT spikes decrease transmission. Due to the incidence angles of the backlighter and drive profiles, a great deal of the undriven target is also illuminated in each image, indicated by the smooth portions of the backlit regions. These regions provide relatively unperturbed images to estimate the backlighters' profiles, allowing the transmission, T, and optical depth (OD),  $\tau = -\ln(T)$ , of each system to be inferred. The optical depth is of particular interest because it is roughly proportional to the height h of the perturbations,  $\tau \approx \rho \mu h$ 

where  $\rho$  is the average density and  $\mu$  is the average opacity of the compressed, unablated target [25–27].

A similar analysis was applied to these radiographs to that detailed in Refs. [20, 28, 29], and a summary of this process is shown in Fig. 2 for a magnetized (top) and unmagnetized (bottom) target 2.4 ns into the main drive. To begin, average signal and noise images were required to apply a Wiener deconvolution algorithm [28, 30]. To this end, the backlighter's spatial profile was estimated by fitting a rotatable, elliptical super-Gaussian to the undriven portions of the images. This fit was simultaneously applied to all 16 sub-images per shot, maintaining the same super-Gaussian shape but allowing the amplitude to vary between sub-images. This method took advantage of the parallax of the backlighter and drive to provide a reliable fit for each shot. The resulting backlighter profiles were used to infer target transmission [Figs. 2(b) and 2(g)]. Adjacent transmission images within a strip were correlated together and used to produce transmission signal and noise images through addition and subtraction, respectively. These images were then multiplied by the average backlighter profile to produce radiographic signal and noise images. This process resulted in three signal and noise images per strip to analyze.

To ensure the same region was analyzed at all times, images across strips were correlated together and cropped to the central  $450 \,\mu\text{m} \times 450 \,\mu\text{m}$  region of the backlighter and drive (Figs. 2(c) and 2(h)). Using the estimated noise profiles, a Wiener deconvolution algorithm was applied to the radiographic signals, compensating for the

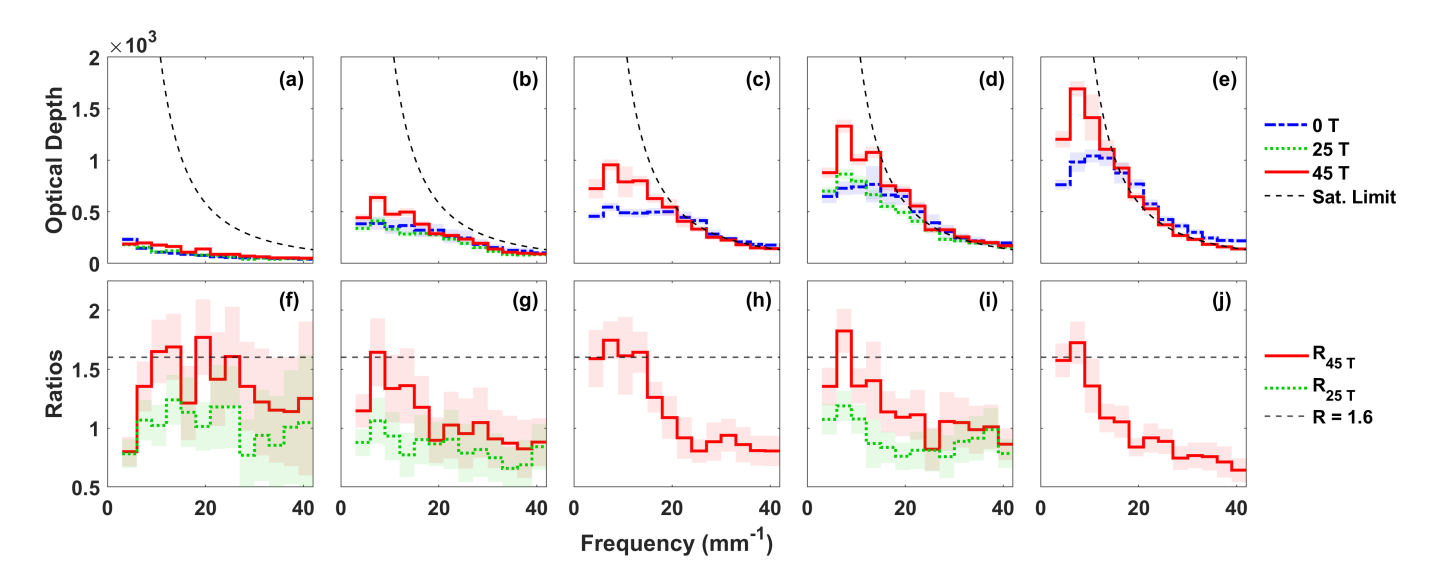


FIG. 3. [(a)-(e)] The average Fourier spectra for each imposed field strength at (a) 1.2 ns, (b) 2.0 ns, (c) 2.4 ns, (d) 2.8 ns, and (e) 3.2 ns. The estimated saturation limit is included for visual reference. Note that no 25 T data were acquired at the times plotted in (c) and (e). [(f)-(j)] The ratio of the average 45 T (red) and 25 T (green dotted) spectra to the average 0 T spectrum. The horizontal dashed line indicates the  $\sim 60\%$  increased signal in the unsaturated modes of the 45-T spectra. The shaded regions represent the uncertainties and are driven primarily by shot-to-shot variations, particularly at low signal levels.

blurring effects of the imaging system and reducing noise [31]. In this process, noise uncertainties were calculated following the methods of Ref. [28], though these proved to be negligible in the regions of interest. As can be seen in Figs. 2(d) and 2(i), the deconvolution process sharpened small-wavelength features while limiting noise. It is also evident from these images that the magnetized targets had significantly increased perturbation levels compared to their unmagnetized counterparts, indicating either faster RT growth or greater imprint levels.

To quantify this comparison and distinguish between these two effects, the deconvolved images were converted to OD once again using the average backlighter profiles. A 2D Fourier transform was applied to the OD images, and the Fourier amplitudes were azimuthally averaged into frequency bins to examine the average OD amplitude as a function of frequency. Each signal-noise image pair within a strip was individually analyzed, and the variation between the three resulting spectra was taken to be the uncertainty for that strip. Figs. 2(e) and 2(j) show the spectral evolution of the examples. To provide a visual reference, a curve proportional to the Haan saturation limit is included [32]. This limit is the theoretical amplitude at which RT growth is expected to enter its nonlinear phase, breaking from exponential growth. In terms of bubble height, it is given by  $S_k = 2/Lk^2$  where  $L = 450 \,\mu\text{m}$  is the geometric average dimension of the image and k is the perturbation wave number [33–35]. As stated previously, the precise constant of proportionality between bubble height and OD is the target's average density and opacity, but these are experimentally unknown. Instead, the cold opacity of CH to 1.4 keV x rays,  $\mu = 788 \,\mathrm{cm}^2/\mathrm{g}$ , and a compressed density of  $\rho = 3 \,\mathrm{g/cm}^3$ 

were chosen to provide an estimation of this curve. While these values of  $\rho$  and  $\mu$  are physically reasonable [23], this curve should be taken primarily as a visual reference.

As can be seen from these images, the modes grew in both cases until they approached the Haan-type curve, at which point they stagnated. This is similar to the behavior of saturated modes seen in similar experiments [27, 34, 36], although due to the uncertainty in the conversion factor, it can only be stated that this behavior occurs at some point proportional to this limit. The observed spectra had  $\sim 15\%$  shot-to-shot variation at each frequency on average, with greater signals producing less variation, dominating other sources of uncertainty. This serves as an upper limit for the variation in initial imprint spectra between shots. By 4.0 ns, the spectra began to decrease, indicating perforation of the foil [20, 26]. As a result, the rest of the analysis will focus only on times prior to 4.0 ns.

## IV. COMPARISONS AND DISCUSSION

# A. Separating imprint from RT growth

As stated above, prior to nonlinearity, modes are amplified exponentially in time by the RT instability. Let

$$\Phi(t) = \psi \ e^{\gamma t} \tag{2}$$

be the time-dependent perturbation spectrum,  $\gamma$  the ablative RT growth rate theoretically given by Eq. 1, and  $\psi$  be its initial value, largely determined by imprint, though other factors such as surface roughness will also contribute [37]. The ratio of the magnetized (subscript M)

and unmagnetized (subscript U) spectra is given by:

$$R \equiv \frac{\Phi_M}{\Phi_U}(t) = \frac{\psi_M}{\psi_U} \exp[(\gamma_M - \gamma_U)t]$$
 (3)

 $\psi_M/\psi_U$  is roughly the imprint ratio and is time-independent, while  $\exp[(\gamma_M - \gamma_U)t]$  is determined by RT and is purely time dependent. Therefore, examining the ratio of the spectra gives separable measurements of the two effects.

To capture this information, spectra taken at the same time with the same field strength were averaged together, giving the average behavior of the magnetized and unmagnetized systems. Fig. 3 shows the (top) spectra and (bottom) corresponding ratios of the average spectra at various time steps. As before, in both scenarios, the modes saturate when they approach the Haan-type curve. As a result, their ratios drop to unity as they approach this limit. This is seen, for example, at frequencies greater than  $\sim 18 \, \mathrm{mm}^{-1}$  in Fig. 3(h). However, the ratio of unsaturated modes remains roughly constant at  $R_{45\,\mathrm{T}} \approx 1.6$  at all times. There is no evidence of exponential temporal dependence for this ratio; therefore, the growth rates and one-dimensional (1D) hydrodynamics must be similar at these frequencies. This assertion will be further supported in the following subsection. Tellingly, this ratio is present at 1.2 ns, just 200 ps after simulations expect the target to begin accelerating. [20]. This minimizes the impact of the RT instability, since its growth occurs only under the effect of acceleration. Thus, imprint is determined to have been amplified by the 45 T magnetic fields by  $60 \pm 13\%$ .

Interestingly, when a similar analysis was applied to shot 38190, which had 25 T fields, its spectrum was consistent with the unmagnetized case. Magnetic amplification of the laser imprint only becomes apparent between 25 T and 45 T. This is explained by the Hall Parameter – the ratio of the electron gyrofrequency and the electronion collision frequency – which measures the magnetization of a plasma and is proportional to the magnetic field strength [38]. Pre-shot simulations show that by reducing the field strength from 45 T to 25 T, the Hall parameter decreased from 1.2 to 0.3, implying that electron motion is dominated by particle collisions rather than magnetic effects at the lower field strength.

## B. RT-growth estimates

To support the assertion that the growth rates were similar between the magnetized and unmagnetized cases, two additional arguments are born by the data: the growth of individual modes show similar exponential growth rates below the saturation limit, and the time-averaged growth rates are similar, if not greater in the unmagnetized case.

For the first of these points, Fig. 4 shows the growth of individual perturbation modes in logarithmic scale as

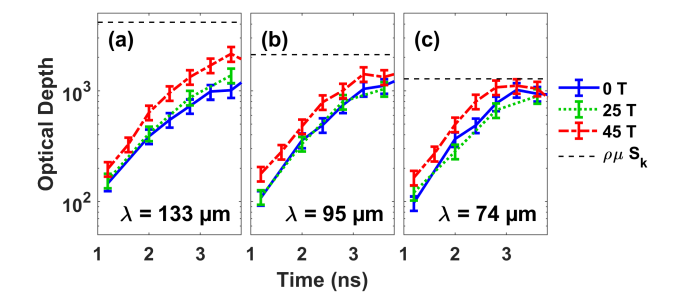


FIG. 4. The average Fourier spectra at each imposed field strength are shown in logarithmic scale as a function of time for frequency bins (a) 6 to  $9\,\mathrm{mm}^{-1}$ , (b) 9 to  $12\,\mathrm{mm}^{-1}$ , and (c)12 to  $15\,\mathrm{mm}^{-1}$ . The average wavelengths  $\lambda$  of these frequency bins are labeled.

a function of time. Prior to both saturation and perforation, all modes grow approximately exponentially, as would be expected for the RT instability. As the modes approach the Haan saturation limit, shown as a horizontal black dashed line in the figure, the perturbations cease growth. Fitting an exponential function to each curve prior to saturation shows strong agreement between the growth rates at all perturbation modes below 21 mm<sup>-1</sup>. The variation of the slopes is 5% between the unmagnetized and 45 T growth rates, well within the fitting errors and measurement uncertainties. At these frequencies, the 45 T amplitudes remain  $60 \pm 13\%$  greater than the unmagnetized amplitudes at all times prior to saturation and perforation, consistent with increased imprint. Projecting these curves back to 1 ns, where RT is expected to begin, clearly shows that this trend should hold.

Second, the time-averaged RT growth rate can be inferred from the spectra. Dividing the spectrum in Eq. 2 by itself at two different times,  $t_1$  and  $t_2$ , and solving for  $\gamma$  gives the inferred time-averaged growth rate:

$$\langle \gamma \rangle (t_1, t_2) = \frac{\ln \left[ \Phi(t_2) / \Phi(t_1) \right]}{t_2 - t_1}$$
 (4)

Fig. 5 shows the inferred growth rates at various times  $t_2$ relative to the earliest acquisition time,  $t_1 = 1.2 \,\mathrm{ns}$ . The growth rates are consistent with the Betti-Takabe growth rate, using  $g = 70 \,\mu\text{m/ns}^2$  and  $L_{\text{min}} = 8 \,\mu\text{m}$  as average values from coarse 1D Gorgon-Chimera simulations of the 45 T initial field strength. [39–41] Due to the size of the grid in these simulations, ablation velocity could not be directly estimated from the simulations with any certainty, but the used value of  $V_a = 3.5 \,\mu\text{m/ns}$  is physically reasonable compared to previous publications.[20, 42] The time-averaged growth rate decreases at later times for two reasons. First, the density scale lengths are expected to increase, damping ablative RT growth. More importantly, though, is the saturated modes cease meaningfully growing beyond the saturation limit. As a result, because the numerator is stagnant in Eq. 4 while the denominator continues to increase, the time-averaged growth rate will decrease at later times.

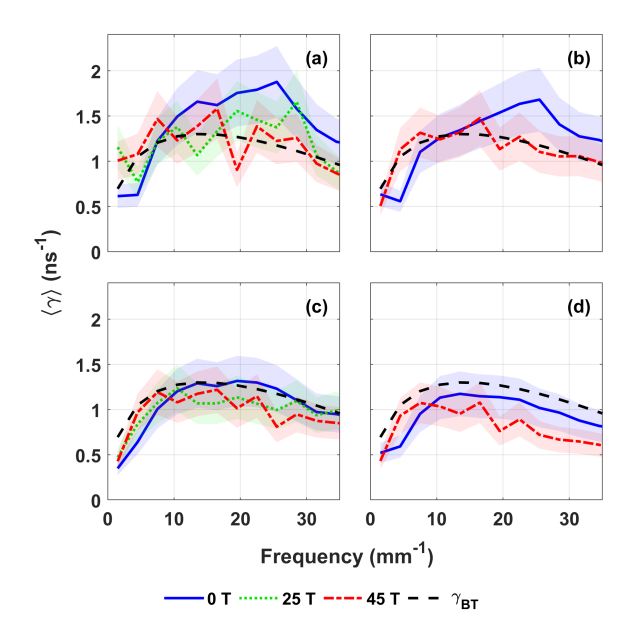


FIG. 5. Inferred time-averaged growth rates at (a)  $2.0\,\mathrm{ns}$ , (b)  $2.4\,\mathrm{ns}$ , (c)  $2.8\,\mathrm{ns}$ , and (d)  $3.2\,\mathrm{ns}$  relative to the earliest spectra acquired at  $1.2\,\mathrm{ns}$  for each imposed field strength. Shaded regions around the lines indicate uncertainties. The estimated Betti-Takabe growth rate is included for comparison.

From these curves, it is clear that all three initial field strengths showed comparable Rayleigh-Taylor growth from their earliest measured spectra. Of the three initial field strengths, it is the unmagnetized case, rather than the 45 T fields, that has the greatest inferred growth rate, albeit with overlapping uncertainties. This is opposite of what would be required for the increased perturbations seen in the 45 T targets to be attributed to RT growth. This strongly supports the argument that the increased perturbations in a 45 T field are due to laser imprint.

## C. Discussion

It should be noted that a 60% increase in laser imprint, while clear and consistent in the data, falls significantly below the pre-shot predictions of *Gorgon-Chimera* simulations where the increase was expected of the order of 200%. Several factors can influence this. The simulations in this paper included a heat-flow and Nernst flux-limiter. For the fields to amplify imprint, they must remain in the conduction zone. As such, these results are sensitive to numerical parameters such as the Nernst flux limiter [43] and transport coefficients [44]. Laser drive is modeled in these simulations using ray tracing with a finite number of rays, and imprint is estimated by varying the energy of individual rays. Anisotropic thermal conduction is then modeled by *Gorgon*. All of these models must be benchmarked against the results presented here.

Recent advances have been made to the treatment of

magnetized heat-flow and Nernst in the transition to the kinetic regime. [45] That work suggests that a geometric average should be employed instead of a hard-cutoff used in most rad-hydro codes. That work also shows that a correction to the mean-free path using the Larmor radius scale-length would improve agreement. Future simulation effort will address these sensitivities in the scenario of magnetized imprint and will be published upon completion. Additionally, new experiments have been designed that will provide further data points for this study into the underlying fundamental physics. These include varying the SSD bandwidth to observe any change in the amplification magnitude or threshold and rotating the magnetic fields to be parallel to the target's surface. Such numerical and experimental studies will provide insights into the detailed underlying physics of magnetic-field advection and its competition with bulk plasma flows in multiple geometries.

#### V. CONCLUSIONS

An experimental campaign was conducted measuring the growth of laser imprint on planar targets when magnetic fields up to 45 T were applied normal to the target's surface. Face-on radiography was used to measure the optical depth of the targets and was spectrally analyzed. The results showed increased perturbations when 45 T fields were applied compared to unmagnetized targets. No discernible difference was observed between the unmagnetized targets and targets with a 25 T imposed field. By comparing the ratios of the spectra at various times, it was concluded that the increased perturbations were due to laser imprint rather than subsequent Rayleigh-Taylor growth. This was supported by analyzing the growth rates of individual modes and inferring the time-averaged growth rates for each imposed field strength. Individual modes were seen to grow at comparable rates before stagnating at the Haan saturation limit. The time-averaged growth rates were comparable at all three magnetization levels, with slightly increased rates inferred in the unmagnetized case. The  $60 \pm 13\%$  increase in laser-imprint perturbations was attributed to a suppression of transverse thermal conduction through the conduction zone, limiting the effects of thermal smoothing when the Hall parameter exceeds unity. This is less than the expected increase in laser imprint of 200% seen in simulations, potentially due to numerical parameters such as the Nernst flux limiter or unresolved advection of magnetic fields out of the conduction zone. These discrepancies will be the subject of future numerical studies.

## ACKNOWLEDGMENTS

This material is based upon work supported by the Department of Energy [National Nuclear Security Administration] University of Rochester "National Inertial

Confinement Program" under Award Number(s) DE-NA0004144. Additionally, this work was partially performed under the auspices of the U.S. Department of Energy by Lawrence Livermore National Laboratory under Contract DE-AC52-07NA27344. This work has also been supported by Research Grant No. PID2022-137632OB-I00 from the Spanish Ministry of Science and Innovation.

This document was prepared as an account of work sponsored by an agency of the United States government. Neither the United States government nor Lawrence Livermore National Security, LLC, nor any of their employees makes any warranty, expressed or implied, or assumes any legal liability or responsibility for the accuracy, com-

pleteness, or usefulness of any information, apparatus, product, or process disclosed, or represents that its use would not infringe privately owned rights. Reference herein to any specific commercial product, process, or service by trade name, trademark, manufacturer, or otherwise does not necessarily constitute or imply its endorsement, recommendation, or favoring by the United States government or Lawrence Livermore National Security, LLC. The views and opinions of authors expressed herein do not necessarily state or reflect those of the United States government or Lawrence Livermore National Security, LLC, and shall not be used for advertising or product endorsement purposes.

- [1] J. Nuckolls, L. Wood, A. Thiessen, and G. Zimmerman, Laser compression of matter to super-high densities: Thermonuclear (ctr) applications pressure: Implosion, ablation (1972).
- [2] S. Atzeni and J. M. ter Vehn, *The Physics of Inertial Fusion* (Oxford University Press, 2004).
- [3] R. Betti and O. A. Hurricane, Inertial-confinement fusion with lasers, Nature Physics 12, 435 (2016).
- [4] R. C. Kirkpatrick, I. R. Lindemuth, and M. S. Ward, Magnetized target fusion: An overview, Fusion Technology 27, 201 (1995).
- [5] P. Y. Chang, G. Fiksel, M. Hohenberger, J. P. Knauer, R. Betti, F. J. Marshall, D. D. Meyerhofer, F. H. Séguin, and R. D. Petrasso, Fusion yield enhancement in magnetized laser-driven implosions, Physical Review Letters 107, 10.1103/PhysRevLett.107.035006 (2011).
- [6] O. V. Gotchev, P. Y. Chang, J. P. Knauer, D. D. Meyerhofer, O. Polomarov, J. Frenje, C. K. Li, M. J. Manuel, R. D. Petrasso, J. R. Rygg, F. H. Séguin, and R. Betti, Laser-driven magnetic-flux compression in high-energy-density plasmas, Physical Review Letters 103, 10.1103/PhysRevLett.103.215004 (2009).
- [7] J. P. Knauer, O. V. Gotchev, P. Y. Chang, D. D. Meyerhofer, O. Polomarov, R. Betti, J. A. Frenje, C. K. Li, M. J. Manuel, R. D. Petrasso, J. R. Rygg, and F. H. Śguin, Compressing magnetic fields with high-energy lasers (2010).
- [8] M. Hohenberger, P. Y. Chang, G. Fiksel, J. P. Knauer, R. Betti, F. J. Marshall, D. D. Meyerhofer, F. H. Séguin, and R. D. Petrasso, Inertial confinement fusion implosions with imposed magnetic field compression using the omega laser, Physics of Plasmas 19, 10.1063/1.3696032 (2012).
- [9] C. A. Walsh, R. Florido, M. Bailly-Grandvaux, F. Suzuki-Vidal, J. P. Chittenden, A. J. Crilly, M. A. Gigosos, R. C. Mancini, G. Pérez-Callejo, C. Vlachos, C. McGuffey, F. N. Beg, and J. J. Santos, Exploring extreme magnetization phenomena in directly driven imploding cylindrical targets, Plasma Physics and Controlled Fusion 64, 10.1088/1361-6587/ac3f25 (2022).
- [10] A. Bose, J. Peebles, C. A. Walsh, J. A. Frenje, N. V. Kabadi, P. J. Adrian, G. D. Sutcliffe, M. Gatu Johnson, C. A. Frank, J. R. Davies, R. Betti, V. Y. Glebov, F. J. Marshall, S. P. Regan, C. Stoeckl, E. M. Campbell, H. Sio, J. Moody, A. Crilly, B. D. Appelbe, J. P. Chit-

- tenden, S. Atzeni, F. Barbato, A. Forte, C. K. Li, F. H. Seguin, and R. D. Petrasso, Effect of strongly magnetized electrons and ions on heat flow and symmetry of inertial fusion implosions, Phys. Rev. Lett. **128**, 195002 (2022).
- [11] R. S. Craxton, K. S. Anderson, T. R. Boehly, V. N. Goncharov, D. R. Harding, J. P. Knauer, R. L. Mc-Crory, P. W. McKenty, D. D. Meyerhofer, J. F. My-att, A. J. Schmitt, J. D. Sethian, R. W. Short, S. Skupsky, W. Theobald, W. L. Kruer, K. A. Tanaka, R. Betti, T. J. B. Collins, J. A. Delettrez, S. X. Hu, J. A. Marozas, A. V. Maximov, D. T. Michel, P. B. Radha, S. P. Regan, T. C. Sangster, W. Seka, A. A. Solodov, J. M. Soures, C. Stoeckl, and J. D. Zuegel, Direct-drive inertial confinement fusion: A review, Physics of Plasmas 22, 110501 (2015).
- [12] F. H. Séguin, C. K. Li, J. L. DeCiantis, J. A. Frenje, J. R. Rygg, R. D. Petrasso, F. J. Marshall, V. Smalyuk, V. Y. Glebov, J. P. Knauer, T. C. Sangster, J. D. Kilkenny, and A. Nikroo, Effects of fuel-capsule shimming and drive asymmetry on inertial-confinement-fusion symmetry and yield, Physics of Plasmas 23, 10.1063/1.4943883 (2016).
- [13] C. Walsh, A. Crilly, and J. Chittenden, Magnetized directly-driven icf capsules: increased instability growth from non-uniform laser drive, Nuclear Fusion 60, 106006 (2020).
- [14] R. L. McCrory, D. D. Meyerhofer, R. Betti, R. S. Craxton, J. A. Delettrez, D. H. Edgell, V. Y. Glebov, V. N. Goncharov, D. R. Harding, D. W. Jacobs-Perkins, J. P. Knauer, F. J. Marshall, P. W. McKenty, P. B. Radha, S. P. Regan, T. C. Sangster, W. Seka, R. W. Short, S. Skupsky, V. A. Smalyuk, J. M. Soures, C. Stoeckl, B. Yaakobi, D. Shvarts, J. A. Frenje, C. K. Li, R. D. Petrasso, and F. H. Seguin, Progress in direct-drive inertial confinement fusion, Physics of Plasmas 15, 055503 (2008).
- [15] S. E. Bodner, Critical elements of high gain laser fusion (1981).
- [16] V. N. Goncharov, S. Skupsky, T. R. Boehly, J. P. Knauer, P. McKenty, V. A. Smalyuk, R. P. J. Town, O. V. Gotchev, R. Betti, and D. D. Meyerhofer, A model of laser imprinting, Physics of Plasmas 7, 2062 (2000).
- [17] G. Fiksel, A. Agliata, D. Barnak, G. Brent, P. Y. Chang, L. Folnsbee, G. Gates, D. Hasset, D. Lonobile, J. Magoon, D. Mastrosimone, M. J. Shoup, and R. Betti, Note: Experimental platform for magnetized high-

- energy-density plasma studies at the omega laser facility, Review of Scientific Instruments 86, 10.1063/1.4905625 (2015).
- [18] L. J. Waxer, M. J. Guardalben, J. H. Kelly, B. E. Kruschwitz, J. Qiao, I. A. Begishev, J. Bromage, C. Dorrer, J. L. Edwards, L. Folnsbee, S. D. Jacobs, R. Jungquist, T. J. Kessler, R. W. Kidder, S. J. Loucks, J. R. Marciante, D. N. Maywar, R. L. McCrory, D. D. Meyerhofer, S. F. Morse, A. V. Okishev, J. B. Oliver, G. Pien, J. Puth, and A. L. Rigatti, The omega ep high-energy, short-pulse laser system (Optical Society of America, 2008) p. JThB1.
- [19] S. Skupsky, R. W. Short, T. Kessler, R. S. Craxton, S. Letzring, and J. M. Soures, Improved laser-beam uniformity using the angular dispersion of frequencymodulated light, Journal of Applied Physics 66, 3456 (1989).
- [20] L. Ceurvorst, R. Betti, A. Casner, V. Gopalaswamy, A. Bose, S. X. Hu, E. M. Campbell, S. P. Regan, C. A. McCoy, M. Karasik, J. Peebles, M. Tabak, and W. Theobald, Hybrid target design for imprint mitigation in direct-drive inertial confinement fusion, Physical Review E 101, 063207 (2020).
- [21] L. Rayleigh, Analytic solutions of the rayleigh equation for linear density profiles, Proceedings of London Mathematical Society XIV, 170 (1883).
- [22] R. Betti, V. N. Goncharov, R. L. McCrory, and C. P. Verdon, Growth rates of the ablative rayleigh-taylor instability in inertial confinement fusion, Physics of Plasmas 5, 1446 (1998).
- [23] C. Mailliet, E. L. Bel, L. Ceurvorst, S. F. Khan, D. Martinez, T. Goudal, N. Izumi, D. Kalantar, P. D. Nicola, J. M. D. Nicola, I. Igumenshchev, V. T. Tikhonchuk, B. Remington, V. A. Smalyuk, L. Masse, and A. Casner, Long-duration direct drive hydrodynamics experiments on the national ignition facility: Platform development and numerical modeling with chic, Physics of Plasmas 26, 082703 (2019).
- [24] D. K. Bradley, P. M. Bell, O. L. Landen, J. D. Kilkenny, and J. Oertel, Development and characterization of a pair of 30–40 ps x-ray framing cameras, Review of Scientific Instruments 66, 716 (1995).
- [25] D. Oron, L. Arazi, D. Kartoon, A. Rikanati, U. Alon, and D. Shvarts, Dimensionality dependence of the rayleigh-taylor and richtmyer-meshkov instability latetime scaling laws, Physics of Plasmas 8, 2883 (2001).
- [26] O. Sadot, V. A. Smalyuk, J. A. Delettrez, D. D. Meyerhofer, T. C. Sangster, R. Betti, V. N. Goncharov, and D. Shvarts, Observation of self-similar behavior of the 3d, nonlinear rayleigh-taylor instability, Physical Review Letters 95, 265001 (2005).
- [27] V. A. Smalyuk, O. Sadot, J. A. Delettrez, D. D. Meyer-hofer, S. P. Regan, and T. C. Sangster, Fourier-space non-linear rayleigh-taylor growth measurements of 3d laser-imprinted modulations in planar targets, Physical Review Letters 95, 215001 (2005).
- [28] V. A. Smalyuk, T. R. Boehly, L. S. Iwan, T. J. Kessler, J. P. Knauer, F. J. Marshall, D. D. Meyerhofer, C. Stoeckl, B. Yaakobi, and D. K. Bradley, Fourier-space image processing for spherical experiments on omega (invited), Review of Scientific Instruments 72, 635 (2001).
- [29] L. Ceurvorst, S. Khan, C. Mailliet, D. Martinez, N. Izumi, P. D. Nicola, J. D. Nicola, T. Goudal, V. Bouffetier, D. Kalantar, I. Igumenshchev, E. L. Bel, B. Rem-

- ington, L. Masse, V. Smalyuk, and A. Casner, Post-processing of face-on radiographic images for quantitative analysis in ablative rayleigh-taylor instability experiments, High Energy Density Physics **37**, 100851 (2020).
- [30] W. H. Press, S. A. Teukolsky, W. T. Vetterling, and B. P. Flannery, Numerical Recipes: The Art of Scientific Computing, 3rd ed., edited by L. Cowles and A. Harvey (Cambridge University Press, 2007) pp. 649–651.
- [31] V. A. Smalyuk, T. R. Boehly, D. K. Bradley, J. P. Knauer, and D. D. Meyerhofer, Characterization of an x-ray radiographic system used for laser-driven planar target experiments, Review of Scientific Instruments 70, 647 (1999).
- [32] S. W. Haan, Onset of nonlinear saturation for rayleightaylor growth in the presence of a full spectrum of modes, Physical Review A 39, 5812 (1989).
- [33] V. A. Smalyuk, O. Sadot, R. Betti, V. N. Goncharov, J. A. Delettrez, D. D. Meyerhofer, S. P. Regan, T. C. Sangster, and D. Shvarts, Rayleigh-taylor growth measurements of three-dimensional modulations in a nonlinear regime, Physics of Plasmas 13, 1 (2006).
- [34] D. A. Martinez, V. A. Smalyuk, J. O. Kane, A. Casner, S. Liberatore, and L. P. Masse, Evidence for a bubblecompetition regime in indirectly driven ablative rayleightaylor instability experiments on the nif, Physical Review Letters 114, 215004 (2015).
- [35] A. Casner, C. Mailliet, S. F. Khan, D. Martinez, N. Izumi, D. Kalantar, P. D. Nicola, J. M. D. Nicola, E. L. Bel, I. Igumenshchev, V. T. Tikhonchuk, B. A. Remington, L. Masse, and V. A. Smalyuk, Long-duration planar direct-drive hydrodynamics experiments on the nif, Plasma Physics and Controlled Fusion 60, 014012 (2018).
- [36] A. Casner, C. Mailliet, G. Rigon, S. Khan, D. Martinez, B. Albertazzi, T. Michel, T. Sano, Y. Sakawa, P. Tzeferacos, D. Lamb, S. Liberatore, N. Izumi, D. Kalantar, P. D. Nicola, J. D. Nicola, E. L. Bel, I. Igumenshchev, V. Tikhonchuk, B. Remington, J. Ballet, E. Falize, L. Masse, V. Smalyuk, and M. Koenig, From icf to laboratory astrophysics: ablative and classical rayleigh-taylor instability experiments in turbulent-like regimes, Nuclear Fusion 59, 032002 (2018).
- [37] J. P. Knauer, R. Betti, D. K. Bradley, T. R. Boehly, T. J. B. Collins, V. N. Goncharov, P. W. McKenty, D. D. Meyerhofer, V. A. Smalyuk, C. P. Verdon, S. G. Glendinning, D. H. Kalantar, and R. G. Watt, Singlemode, rayleigh-taylor growth-rate measurements on the omega laser system, Physics of Plasmas 7, 338 (2000).
- [38] J. D. Huba, NRL Plasma Formulary, Vol. 6790 (Naval Research Laboratory, 1998) pp. 98–358.
- [39] A. Ciardi, S. V. Lebedev, A. Frank, E. G. Blackman, J. P. Chittenden, C. J. Jennings, D. J. Ampleford, S. N. Bland, S. C. Bott, J. Rapley, G. N. Hall, F. A. Suzuki-Vidal, A. Marocchino, T. Lery, and C. Stehle, The evolution of magnetic tower jets in the laboratory (2007).
- [40] C. A. Walsh, J. P. Chittenden, K. McGlinchey, N. P. Niasse, and B. D. Appelbe, Self-generated magnetic fields in the stagnation phase of indirect-drive implosions on the national ignition facility, Physical Review Letters 118, 10.1103/PhysRevLett.118.155001 (2017).
- [41] K. McGlinchey, B. D. Appelbe, A. J. Crilly, J. K. Tong, C. A. Walsh, and J. P. Chittenden, Diagnostic signatures of performance degrading perturbations in inertial confinement fusion implosions, Physics of Plasmas 25, 10.1063/1.5064504 (2018).

- [42] A. Casner, V. Smalyuk, L. Masse, A. Moore, B. Delorme, D. Martinez, I. Igumenshev, L. Jacquet, S. Liberatore, R. Seugling, C. Chicanne, H. Park, and B. Remington, Design and implementation plan for indirect-drive highly nonlinear ablative rayleigh-taylor instability experiments on the national ignition facility, High Energy Density Physics 9, 32 (2013).
- [43] J. P. Brodrick, M. Sherlock, W. A. Farmer, A. S. Joglekar, R. Barrois, J. Wengraf, J. J. Bissell, R. J. Kingham, D. D. Sorbo, M. P. Read, and C. P. Ridgers, Incor-
- porating kinetic effects on nernst advection in inertial fusion simulations, Plasma Physics and Controlled Fusion **60**, 10.1088/1361-6587/aaca0b (2018).
- [44] J. D. Sadler, C. A. Walsh, and H. Li, Symmetric set of transport coefficients for collisional magnetized plasma, Physical Review Letters 126, 10.1103/Phys-RevLett.126.075001 (2021).
- [45] C. A. Walsh and M. Sherlock, Kinetic corrections to heat-flow and nernst advection for laser heated plasmas, Physics of Plasmas 31, 10.1063/5.0225592 (2024).